



Simultaneous densification and improvement of cold spray additively manufactured Ti-6Al-4 V properties via electro-plastic treatment

Mohammed Abdul Khalik^{1,2} · Saden H. Zahiri² · Syed H. Masood¹ · Stefan Gulizia² · M. Faizan-Ur-Rab² · Suresh Palanisamy¹

Received: 13 February 2023 / Accepted: 4 April 2023
© The Author(s) 2023

Abstract

Large-scale industrial application of additively manufactured (AM) components in general, and specifically cold sprayed additive manufactured (CSAM), is limited due to the nature of this technology and the resulting product's porosity and embrittlement. To improve the final properties of additively manufactured material, many lengthy, complex, or expensive post-treatments have been proposed. Reducing the environmental impact, cost, and time required for additive manufacturing will allow for greater use in industrial applications. A novel thermomechanical treatment known as in situ electro-plastic treatment (ISEPT) is used in this study to treat CSAM Ti-6Al-4 V alloy known as grade 5 titanium. The Ti-6Al-4 V alloy has approximately three times the strength and hardness of commercial purity titanium (CP-Ti) with lower ductility and a dual-phase ($\alpha + \beta$) microstructure that poses challenges during the CSAM process. Compared to CP-Ti, the results showed that CSAM Ti-6Al-4 V presented double the porosity and triple the number of ISEPT passes that presented $\sim 2 \mu\text{m}$ ultra-fine grain microstructure. The ultimate tensile strength (UTS) of the ISEPT material was superior to that of CSAM Ti-6Al-4 V and increased from 184 to 1096 MPa with improved ductility rise from 1.1 up to 8.8%. Six ISEPT passes in air resulted in a slight increase in oxygen from 0.2% in the as-CSAM condition to 0.35%. Tensile properties of the ISEPT material were comparable to wrought Ti-6Al-4 V with 989 MPa UTS and 8.3% elongation. The ISEPT passes consolidated the CSAM ($\alpha + \beta$) dual-phase Ti-6Al-4 V and allowed for the nucleation of equiaxed grains at the vicinity of former CSAM splat boundaries. The formation of lamellar colonies within the splat's inner regions was observed. The role of ISEPT conditions on the rapid elimination of porosity and the evolution of cold spray splat boundaries via dynamic recrystallization were discussed.

Keywords Cold spray additive manufacturing · Thermomechanical treatment · Thermomechanical processing · Grade 5 titanium · Ti-6Al-4 V · Recrystallization · Electroplastic effect

1 Introduction

Grade 5 titanium (Ti-6Al-4 V) is the most commonly used titanium (Ti) alloy and accounts for 50% of total titanium alloys due to its attractive combination of high strength, low density, and corrosion resistance [1]. The other benefits of Ti-6Al-4 V alloy such as biocompatibility, formability, and

better response to heat treatment have been broadly utilised for many commercial applications [1, 2].

Titanium, however, is expensive due to its reactivity to oxygen at high temperatures that requires inert atmosphere or vacuum from upstream sponge production to downstream heat treatment and hot deformation processing [3, 4]. Compared to commercial purity titanium (CP-Ti), the higher strength and lower ductility of Ti-6Al-4 V further increase the downstream manufacturing costs.

One of the potentially cost-effective methods to produce grade 5 Ti components is the cold spray additive manufacturing under atmospheric conditions with reduced environmental impact and capital cost (CSAM) [5]. In the CSAM process, $\sim 5\text{--}70 \mu\text{m}$ size titanium particles are propelled using nitrogen or helium gas to supersonic speeds (500–1500 m/s) through a nozzle and deposited on a substrate without melting

✉ Suresh Palanisamy
spalanisamy@swin.edu.au

¹ School of Engineering, Swinburne University of Technology, John St., Hawthorn, VIC 3122, Australia

² CSIRO Manufacturing, Commonwealth Scientific and Industrial Research Organization, Clayton, VIC 3168, Australia

to produce parts. This is to form a metallurgical bond combined with mechanically interlocking after deposition [5–8]. The outcome of the additive process can be a solid-state 3D structure from deformed and infused powder (splat) [5, 7, 9]. The performance of the CSAM material is controlled by many process parameters, such as the propellant gas pressure, temperature, and its type and the standoff distance between the nozzle and substrate. Powder material, shape, and size have been identified as important factors for successful CSAM deposition [7–9]. All these parameters affect the critical particle velocity that is required for successful cold spray bond formation [9, 10]. The role of each process parameter on critical particle velocity and the resulting CSAM product properties have been intensively studied elsewhere [6–17].

The melt-less CSAM is a high deposition rate additive process with the ability to produce larger-size products while maintaining powder material initial microstructure. However, CSAM generally introduces brittleness and porosity that could present as low as 1% to as high as 10–15% depending on the propellant gas i.e. helium or nitrogen [7]. Helium as a carrier gas, despite its considerably higher cost, increases Ti-6Al-4 V particles velocity significantly above the critical velocity (> 900 m/s) reducing porosity [7, 18]. Elimination of porosity, however, does not overcome the brittleness of CSAM Ti-6Al-4 V that requires further treatment to improve ductility [6]. Some studies have reported successful heat treatment of CSAM grade 5 Ti at 500 to 1000 °C [19–23]. Hot rolling [24, 25], hot isostatic pressing (HIP) [26], shot peening, friction stir processing, and laser post-treatments have been extensively used as post-treatment processes to improve CSAM grade 5 Ti properties [6]. These processes exhibit technological challenges that generally add to the cost of manufacturing. For example, the HIP process, that is considered an effective method of improving Ti-6Al-4 V properties, has a major drawback of high equipment costs in relation to manufactured components size and use of inert gas, in addition to safety concerns [6, 7, 27].

Previous studies suggest that direct resistance heating is highly promising to achieve the best combination of titanium properties compared to the other conventional oven heating and cooling methods such as water quenching [28–34]. The resistive heating followed by air-cooling leads to the formation of fine martensitic microstructure with mechanical properties superior to the costly bimodal $\alpha + \beta$ titanium microstructure [28]. Other studies on titanium alloys including titanium VT6 (the Russian equivalent of Ti-6Al-4 V) included the mechanism and kinetics of phase transformations [35] at higher than β -phase transus temperature. The formation of finer and smaller martensitic β -phase plates and intragrain microstructure, in a significantly shorter time than conventional oven heat treatment, was presented in this study [28]. Another study showed that the growth of Ti-6Al-4 V beta grains within a fully lamellar microstructure balanced the tensile, fatigue, and

creep properties of titanium alloys [36]. The duration of rapid resistive heat treatment must be carefully controlled to avoid excessive grain growth [36, 37]. A similar outcome from other research work was found on RHT on titania tube crystallinity for orthopaedic implant application [38]. The use of electric resistive heating is also utilised to improve Ti-6Al-4 V room formability and near elimination of spring back [39]. A recent study on the use of RHT with Ti-6Al-4 V alloys [40] showed rapid heat treatment from β -phase followed by water quenching resulted in fully martensitic titanium microstructure that enabled refinement of β grain size from 40 to as small as 8 μm . This grain refinement and martensitic transformation led to enhanced strength and ductility when a rapid heating rate of 50 °C/s was used [40].

Electro-plastic treatment (EPT) of Ni-Ti shape memory alloy wires [41, 42] has been shown to be highly effective in the improvement of mechanical properties via the introduction of 25–50 nm nano-size grains [41]. Similar benefits have been reported in other studies [29] [32, 43] [30]. In a recent study on 73% cold rolled CP-titanium sheets, the post-treatment using AC current pulsation initiated static recrystallization [44, 45]. Higher recrystallization was achieved when electro-pulsing was carried out along the rolling direction rather than the transverse direction.

Recently, our studies in relation to in situ electro-plastic treatment (ISEPT) revealed significant improvement in mechanical properties of CSAM CP-Ti [46, 47]. The applied electric current was expected to provide electron wind that contributes to localised joule heating effect through the electrons' interactions with the crystallographic defects such as dislocations, grain boundaries, and other imperfections. Such an effect assists with dislocation motion weakening the electron cloud of metallic bonding [43]. Further recent studies on the electroplasticity phenomenon associated with the electrically assisted manufacturing/forming (EAM/EAF) and side effects such as “skin effect”, and titanium microstructure evolution published elsewhere [48–53]. The alignment of electric current direction with the applied deformational load is believed to provide the synergy that resulted in dynamic recrystallization of the CSAM below titanium-oxygen critical diffusion temperature with details explained elsewhere [46, 47]. The novelty of this work can be expressed by the fact that the simultaneous application of electric current and load facilitated rapid recrystallization (softening) and densification of CSAM Ti-6Al-4 V in air with potential commercial benefits.

The proposed electro-plastic thermomechanical treatment (TMT) could contribute to the establishment of mini-mill plants with a small environmental footprint and significantly reduced capital to manufacture grade 5 titanium. Continuous fabrication is possible via simultaneous robotic CSAM deposition and ISEPT of the grade 5 Ti. Such development demands for understanding of the material microstructure-mechanical property relationship carried out in this study.

Results showed that the ISEPT of CSAM Ti-6Al-4 V differs from CP-Ti that constitutes only α -phase. For example, the higher strength and lower ductility of Ti-6Al-4 V presented higher porosity in the as-sprayed material. The presence of dual ($\alpha + \beta$) phase with higher electric resistivity and lower thermal conductivity improved mechanical properties of grade 5 Ti via the formation of ultrafine (< 5 microns) grains that was not observed in CP-Ti of previous study. Results confirmed that ISEPT's contribution to the improvement of CSAM robotic additive manufactured grade 5 Ti strength was a considerably demanding detailed investigation of complicated microstructure evolution.

2 Materials and methods

2.1 The ISEPT machine

The ISEPT machine used in this research was developed at Commonwealth Science and Industrial Research Organisation (CSIRO), under patent number WO2018232451 [14]. The schematic diagram in Fig. 1 describes the ISEPT

machine with further analysis of the process parameters published elsewhere [46, 47]. The applied current used in treating CSAM Ti-6Al-4 V was 1.5 kAmp with a rolling surface speed of 0.4 mm/s, and 0.7 MPa was the maximum load of the designed machine. The specimen temperature was measured using an aT1050sc FLIR IR camera (Oregon, USA). The CSAM Ti-6Al-4 V strips were machined to the required cross-section of 3.5×3.5 mm and 70 mm long for ISEPT treatment, as seen in Fig. 1c. Experimental trials showed that 3.5×3.5 mm cross-section corresponding to $h_0 \times w_0$ in Fig. 1b initiated sufficient deformation and reduction under maximum applied load (0.7 MPa) in CSAM Grade 5 Ti. Maximum of six successive passes were used at 1.5 kAmp, 0.4 mm/s rolling surface speed (RSS), and 0.7 MPa rollers pressure.

2.2 Additive manufacture of Ti-6Al-4 V strips

The CSAM Ti-6Al-4 V strips of 5×5 mm cross-section and a total length of 200 mm were additively manufactured using Plasma Giken® PCS-1000L system (Saitama, Japan), attached to ABB® (Friedberg, Germany) robotic arm to

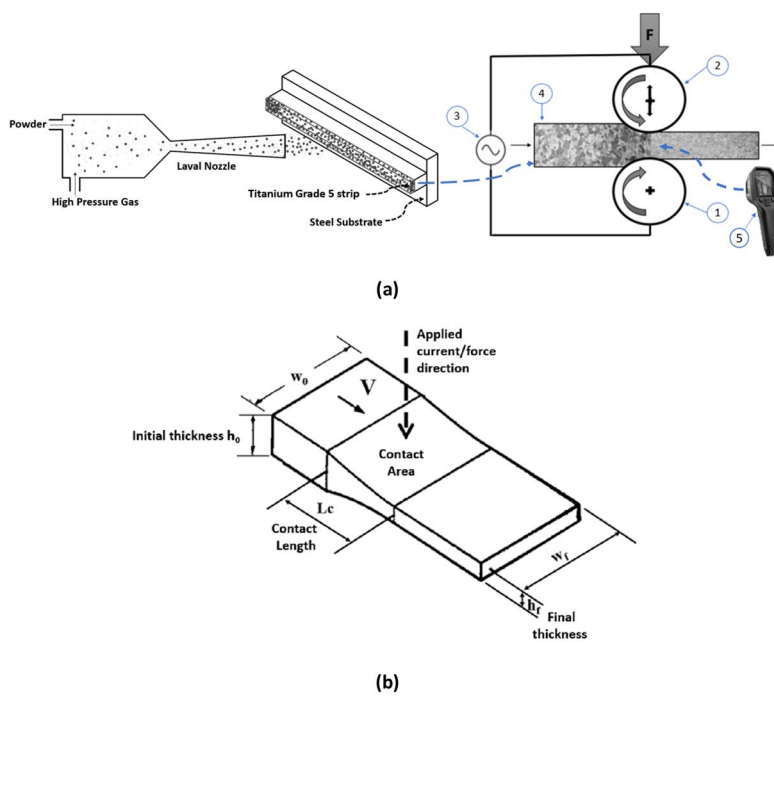


Fig. 1 **a** Schematic diagram of the CS-AM system and the ISEPT machine. (1) Bottom roller, (2) top roller, (3) electric AC power source, (4) conductive specimen, and (5) IR camera. **b** Sample geometry during the ISEPT process including the electric cur-

rent and applied force directions [47]. **c** Images of the CSAM (i–v) and ISEPT process (vi) for producing the 3.5×3.5 mm Ti-6Al-4 V CSAM strips including IR image of the processed strip during ISEPT treatment

precisely control the cold spray nozzle position during the deposition process, as seen in Fig. 1c. The cold spray process parameters (temperature, pressure) were 900 °C, 5 MPa, and 25 mm stand-off-distance (SOD). A developed digital twin for cold spray was used to estimate the state of particles from the injection point to the moment of impact in relation to the powder size distribution of grade 5 Ti supplied by AP&C, Canada. The Cold Spray Digital Twin (CSDT) inputs were similar to the industry scale Plasma Giken® cold spray system of this study that included process temperature, pressure, feed rate, nozzle assembly, and cooling system. The CSDT outputs were according to a validated 3D multicomponent CFD model, ANSYS™ CFX Solver® under Workbench™ version 2021R1 [47, 54–58]. Details of numerical analysis, computational domain, boundary conditions, and particle tracking were published earlier [5, 55, 58]; therefore, a short explanation is provided here.

For the numerical analysis, ANSYS™ CFX Solver® was employed to solve Navier–Stokes equations guided by momentum, continuity, and total energy equations. The 3D computational domain in this study were a solid nozzle, carrier gas (nitrogen), surrounding air, and solid substrate. The substrate was a 70 × 70 × 5 mm stainless-steel square plate [3]. The surrounding domain was a 400 mm diameter and 361.5 mm long cylinder with three vertical faces that were nozzle inlet, substrate surface, and main peripheral surface filled with ambient air.

For the computational grid, ANSYS® elements were hexahedral for both fluid and solid domains, with a combination of lower and larger grid element sizes explored during mesh optimisation. The surrounding cylindrical air domain had 52.3 mm mesh elements. The critical locations were the nozzle throat, jet expansion region near the nozzle exit, and jet impingement zone in front of the substrate. An optimum element size of 0.018 mm was considered for the throat to accommodate gas compression-expansion variations. Near-wall and free-stream turbulence models used inflation layers with an estimated y^+ value of ~5 [59, 60].

As for the particle tracking, nitrogen was used as the carrier gas at 900 °C, 5 MPa (50 bar) pressure, and 25 mm SOD. The interaction between solid particles and propellant gas was defined using the Lagrangian particle tracking approach [54, 61, 62]. The CSDT predicted velocity and temperature for (2 kg/hr) spherical titanium particles based on Ti-6Al-4 V particle size distribution [56, 57, 63] and similar to the Plasma Giken® cold spray system. Fully coupled momentum and heat transfer occurred between propellant gas and solid particles. Details of particle transport equations, including acceleration equation, drag coefficient, drag force, and heat transfer equation, can be found elsewhere [55].

A stainless-steel substrate of 5 × 200 mm was grit blasted and mounted to an ABB robotic arm (Fig. 1). The deposited

strip was manufactured to ~5 mm thickness after 18 passes with 1 mm line spacing, at 200 mm/s robot transverse speed, as seen in Fig. 1c.

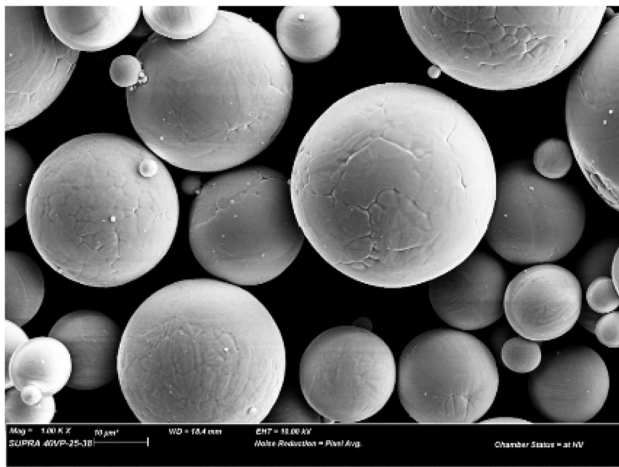
The Ti-6Al-4 V feed stock powder was AP&C Ti ASTM-F2924 (grade 5) with chemical composition as shown in Table 1 and spherical morphology as shown in Fig. 2a. The particle microstructure presented a lamellar morphology as seen in Fig. 2b. The powder size distribution as per ASTM-B822 was D_{10} 20 μm, D_{50} 33 μm, and D_{90} 44 μm, with 3% by volume < 15 μm.

2.3 Characterisation and mechanical testing

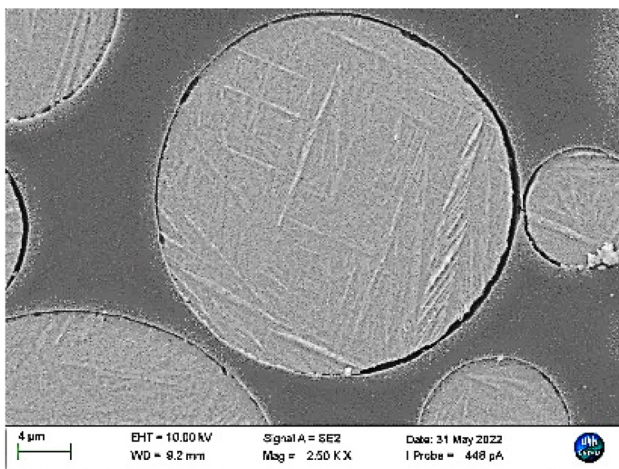
The off-the-shelf (OTS) and CSAM ISEPT-treated Ti-6Al-4 V samples' microstructure was assessed using Olympus GX71 and BX61 optical microscopes. The Ti-6Al-4 V specimens were cut and cold-mounted in epoxy resin. The mounted samples were subjected to progressive grinding to 1200 grit using SiC papers. Further automated polishing was carried out with 15 μm, 3 μm, and 1 μm polishing agents and suitable corresponding polishing cloths. Finally, a minimum of 15 min polishing was carried out using OP-S colloidal silica suspension (0.25 μm) mixed with 10% hydrogen peroxide and 10% ammonia for optical microscopy. This process allowed polarised light optical imaging with improved contrast to reveal grain boundaries of Ti-6Al-4 V samples. Further 10 s etching of selected samples was adopted using Kroll's reagent (3 mL HF, 6 mL HNO₃, 100 mL water) for scanning electron microscope (SEM) observation. Similarly, to reveal remnants of splat boundaries (RSB), Kroll's reagent etching was carried out for 10 s, followed by progressive light polishing with OP-S and MD-CHEM polishing cloth. The sample's porosity was measured using image analysis. Bulk porosity was measured by Archimedes principle method using ASTM-B962-13 procedure [64]. High-resolution SEM images of each condition were used to measure the mean grain size/thickness using the linear intercept method, with each image covering at least 50 grains.

Table 1 Composition of the Ti-6Al-4 V (grade 5) AP&C powder

Powder composition (weight percent)	
Element	Measured wt%
Aluminium (Al)	6.4
Vanadium (V)	4.05
Iron (Fe)	0.19
Oxygen (O)	0.18
Carbon (C)	<0.01
Nitrogen (N)	<0.01
Hydrogen (H)	0.002
Others, total	<0.2
Titanium (Ti)	Balance



(a)



(b)

Fig. 2 SEM images of the AP&C Ti-6Al-4 V grade 5 feed stock powder **a** as received and **b** etched cross-section

The microstructure evolution during the progressive number of ISEPT passes and selected tensile fracture surface of the as-CSAM and ISEPT-treated Ti-6Al-4 V strips were further examined using a ZEISS SUPRA 40 VP scanning electron microscope (SEM). Qualitative chemical analysis was carried out using a Merlin GeminiSEM (Oberkochen, Germany) energy-dispersive X-ray spectroscopy (EDS) system. Oxygen and nitrogen content were determined using a LECO Inert gas Fusion Analyzer Model-ONH836 from LECO Corporation, USA. Using $\text{CuK}\alpha$ radiation (40 kV, 40 mA) in the 2θ range of $5\text{--}130^\circ$ with step size 0.02° , the X-ray peaks of as-CSAM and ISEPT Ti-6Al-4 V samples were revealed using a Bruker D8 Advance A25 XRD (X-ray Diffraction) machine from Bruker Corporation, USA. The crystalline phases were identified using ICDD-JCPDS powder diffraction database using EVATM v6 search match program, and the lattice parameters were determined using Bruker TOPASTM program.

The mechanical properties were evaluated using a Buehler Micromet 2013 Vickers Hardness tester with a load of 300 gf, a dwell time of 10 s, and 10 indents per sample. A 10 kN Instron 5566 universal testing machine, USA was used to assess the tensile properties of Ti-6Al-4 V samples. Waterjet cutting was used due to its convenient for minimisation of residual stress during sample preparation. A Maxiem 1515 abrasive waterjet cutter by Omax, Seattle, USA was used at 50,000 PSI water pressure with the addition of Garnet powder as abrasive agent. The OTS and ISEPT (6 passes) Ti-6Al-4 V tensile specimens were waterjet cut and CNC machined to identical dimensions of 3×1 mm gauge cross-section and total length of 47 mm similar to the previously published work [65]. The as-CSAM Ti-6Al-4 V, however, due to its brittleness, were CNC machined to ASTM-E8 standard tensile specimen dimensions with a 6×2 mm gauge cross-section. To reduce the effect of machining surface roughness and strain, tensile samples were subjected to progressive manual grinding with $500 \mu\text{m}$ SiC grit paper, to minimise variations in surface roughness [66, 67].

3 Results

Recent studies of OTS CP-Ti [46] and CSAM CP-Ti [47] structures revealed the ability of ISEPT to rapidly recrystallise and significantly reduce porosity and brittleness. The limited oxygen pick up reported during the ISEPT process proved the potential for the elimination of protective atmosphere to manufacture Titanium. In this study, cold sprayed Ti-6Al-4 V alloy was subjected to the ISEPT process under atmospheric conditions to investigate cost effective reduction of porosity and embrittlement in the additive structure.

Figures 3 and 4 show results of the cold spray process simulation using CSDT for the Ti-6Al-4 V powder. It is worth noting that the cold spray system (Plasms Giken®) in this study had a different nozzle geometry from the previously published work [47] on CP titanium that used Impact Innovation® cold spray system. Detailed information from CSDT provided the opportunity for optimisation of the deposition conditions in relation to a broad range of commercially available nozzles including Plasms Giken® system. The estimated particle velocities (V_p) for the chosen powder were above the critical velocity (V_c) as shown in Fig. 3b indicating high deposition efficiency. Qualitative analysis of the results in Fig. 4 suggested that the V_p for the majority of large particles, i.e. $+25 \mu\text{m}$, was not substantially above V_c to produce considerable particle deformation. For example, $10 \mu\text{m}$ particles achieved 350 m/s higher velocity than estimated V_c that was $\sim 200 \text{ m/s}$ higher than the $35 \mu\text{m}$ particles (Fig. 4). This suggested the formation of a porous additive structure. This was with the consideration of Ti-6Al-4 V high

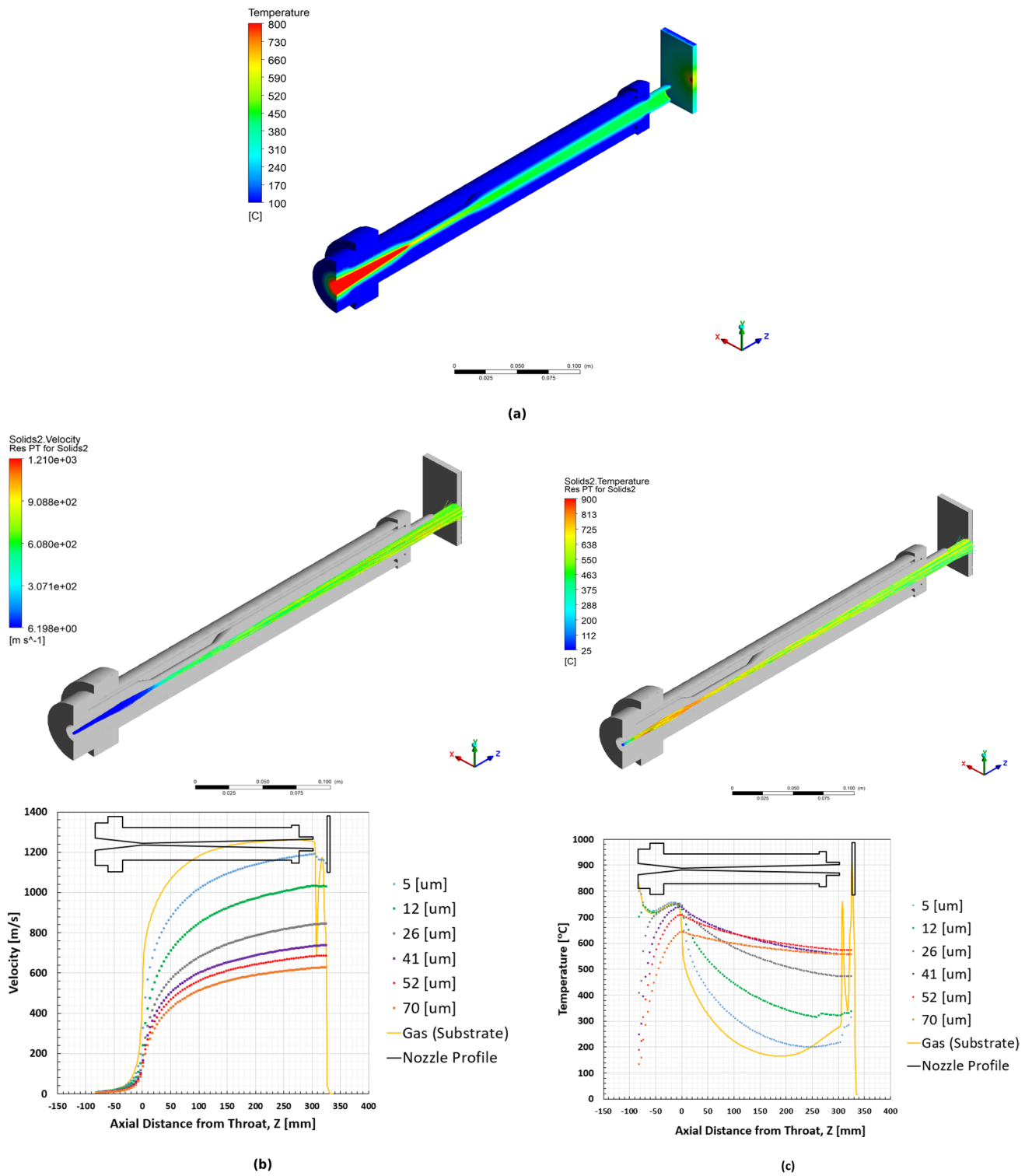
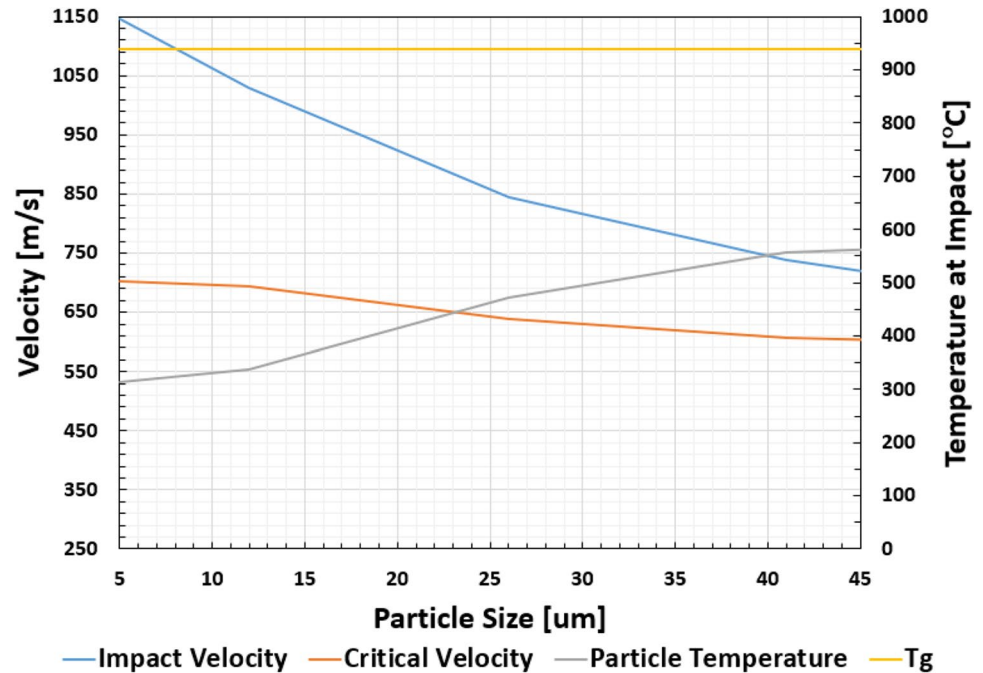


Fig. 3 CSDT estimation of Plasma Giken® cold spray system performance at 900 °C, 5 MPa, and 25 mm SoD cold spray conditions. **a** Glass nozzle assembly temperature profile including cooling system,

b particle velocity profile, and **c** temperature profile of Ti-6Al-4 V particles from injection point to the substrate surface

Fig. 4 Comparison of the CSDT estimated values for V_p , T_p , T_g , and V_c in relation to Ti-6Al-4 V particle size at the moment of impact onto substrate for 900 °C, 5 MPa, and 25 mm SoD cold spray conditions



strength (UTS 950 MPa) that limits particle deformation after impact. The measured porosity was about 13% confirming CSDT estimations. The grade 5 strip had almost 50% higher porosity than CP-Ti with 8% porosity reported in a previous study [47].

The ISEPT process parameters were optimised to 1.5 kAmp, 0.4 mm/s rolling surface speed (RSS), and 0.7 MPa rollers pressure to attain sufficient (i.e. at least 60%) reduction in 3.5×3.5 mm strips. Six successive ISEPT passes were considered to achieve sufficient densification while minimising accumulation of Oxygen in the material under atmospheric conditions. Comparison of the ISEPT parameters in Fig. 5a revealed that a reduction in thickness contributed to an increase in current density. After the fourth ISEPT, variations in strain and strain rate were limited (Fig. 5b) with further details provided elsewhere [46, 47]. The temperature measurement during the first two ISEPT passes was ~816 °C and 948 °C, consecutively. The temperature for the remaining passes was not determined due to reduced sample size below the IR camera precision.

3.1 Evolution of microstructure

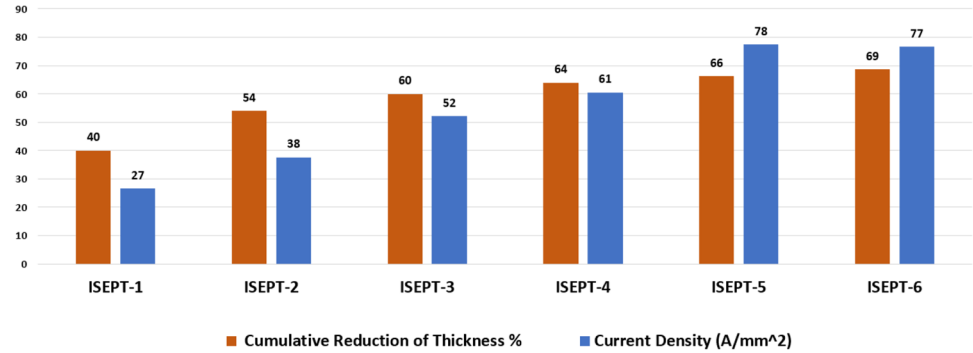
The as-sprayed Ti-6Al-4 V porosity was 13% (Fig. 6) that was higher than 6% for CP-Ti reported in previous work [47]. Figure 6 reveals the CSAM “splats structure” [8] where the deformed feed stock particles bonded through a combination of mechanical interlocking and metallurgical bond formation after supersonic impact and severe plastic

deformation (SPD). In agreement with the qualitative assessment of CSDT simulation, some particles initial spherical shape (arrows in Fig. 6) was almost intact confirming limited deformation of Ti-6Al-4 V that contributed to insufficient densification and presence of pores.

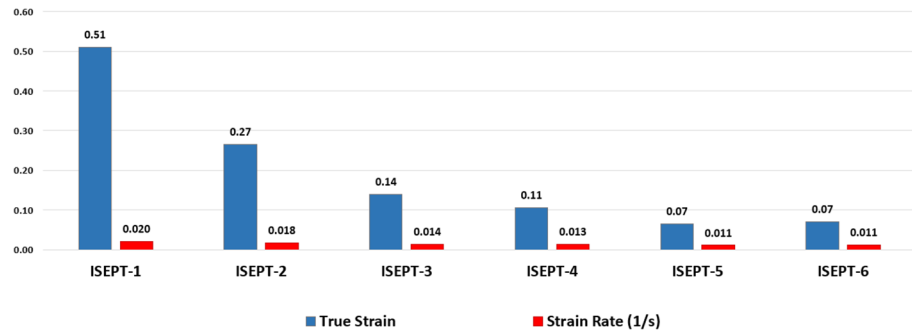
Deformation from six passes led to a total cumulative reduction of 68.6% that corresponded to a considerable reduction in porosity to 0.03% and dynamic recrystallization as seen in Figs. 7, 8, and 9. Figure 7 a, b shows the microstructure after the first pass with partial elimination of splat boundaries, highlighted with orange arrows. Other features observed in this microstructure were RSB and porosity highlighted with white and yellow arrows, respectively. The inner regions of the splats showed the formation of ~1 μm constituents resembling grains shown with red arrows in Fig. 7b. The creation of high dislocation density combined with Joule heating has been reported to originate these fine grains [7, 68]. The microstructure after the second ISEPT pass is shown in Fig. 8. As seen in Fig. 8c, the presence of some pores could act as areas of stress concentration contributing to crack initiation and failure. The presence of porosity and RSB after two ISEPT passes suggested the application of more ISEPT passes for further densification of the additively manufactured grade 5 titanium.

The porosity and RSB were nearly eliminated after six ISEPT passes (Fig. 9a). Only corners of the strip had porosity due to limited deformation that was expected [69, 70]. The Ti-6Al-4 V microstructure showed a unique integration of the two microstructural morphologies, equiaxed grains with necklacing in the original splat boundaries combined

Fig. 5 ISEPT treatment process parameters during the six passes. **a** Reduction of thickness and applied current density and **b** true strain and strain rate



(a)



(b)

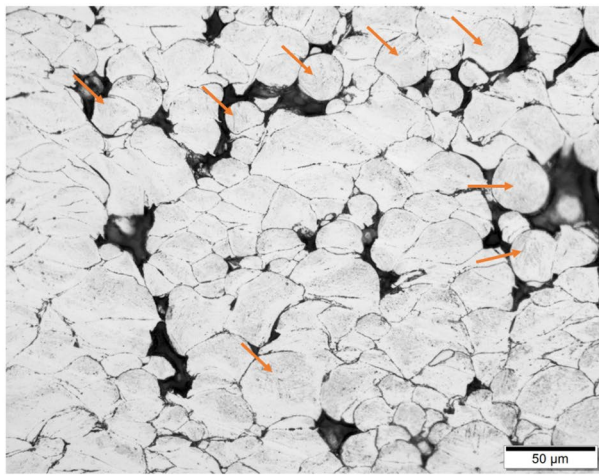
with lamellar colonies in the inner splat regions as seen in Fig. 9b. The dashed yellow lines correspond to original splat boundaries after ISEPT with yellow arrows detailing the lamellar inner region. The equiaxed grains were mainly formed from the highly deformed splat boundaries and their vicinity that were highlighted with red arrows in Fig. 9 b, c.

The severe plastic deformation (SPD) of particles in cold sprayed structure [7, 9] that contributes to splat formation and bonding could be the reason behind the microstructure observed in Fig. 9 b and c. Salandro et al. [43] reported grain boundaries and other crystallographic imperfections act as localised heating zone due to the interactions with electrons wind. Similarly, the splat boundaries in cold spraying are expected to interact with the electron wind resulting in localised heating regions that combined with crystallographic defects acted as nucleation sites for new grains [71]. However, for the inner splat regions, lamellar growth was dominant due to insufficient deformation and dislocation density for nucleation of recrystallised grains. These complicated events need to be systematically studied in the future to determine the relationship between the density of the cold spray splat boundary, magnitude of deformation, and applied current in relation to nucleation and growth of the recrystallised grains in ISEPT microstructure.

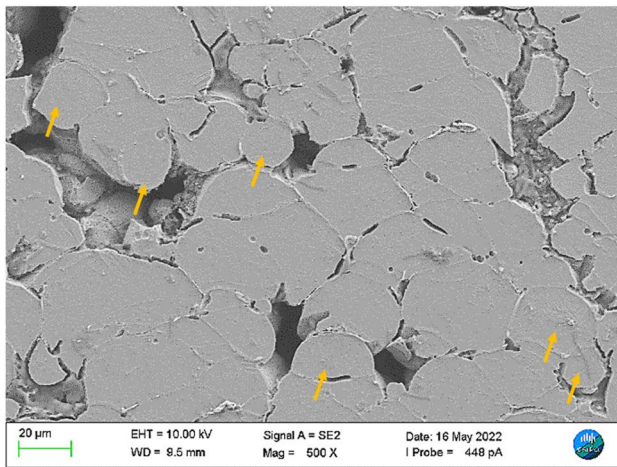
The grain size was measured using image analysis to determine the progress of dynamic recrystallisation in ISEPT

microstructure after each individual passes (Fig. 10a). It is worth noting that a detailed study of the grain and sub-grain formation in ISEPT is the subject of a future study that could reveal the mechanism for the formation of sub-grains with orientation, i.e. less than 15°.

Results showed that ISEPT facilitated the formation of 1–3 μm grains that were considerably finer than OTS Ti-6Al-4 V with generally order of magnitude larger grains. This result confirmed that ISEPT was capable of transforming cold spray splat structure to ultrafine grain (UFG) structure that generally has less than 5 μm grains with improved mechanical properties [29, 37, 42]. Multiple ISEPT passes increased the average UFG size marginally from ~1 to ~3 μm . The volume fraction of porosity was substantially reduced after multiple passes particularly at the centre of the deformed structure to the levels that resembled a fully dense Ti-6Al-4 V structure Fig. 9a and 10b. Combined current and deformational strain that was at its maximum at the centre of the strip was most likely the drive for dynamic recrystallisation and elimination of RSB. This, however, was less effective on the corners of strip as seen in Figs. 7, 8, and 9a, with the presence of RSB and porosity due to smaller strain and barrelling effect [70, 72, 73]. Bulk density measurement of six ISEPT Ti-6Al-4 V samples using the Archimedes principle [64] revealed the presence of ~1% porosity that was sourced from the barrelled corners of specimen after 6 ISEPT passes.



(a)

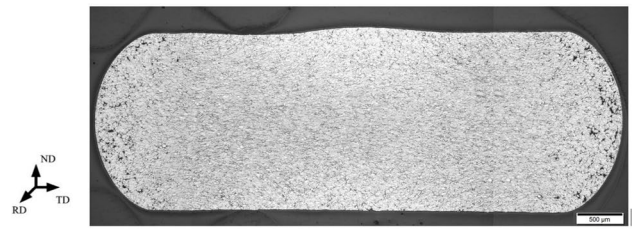


(b)

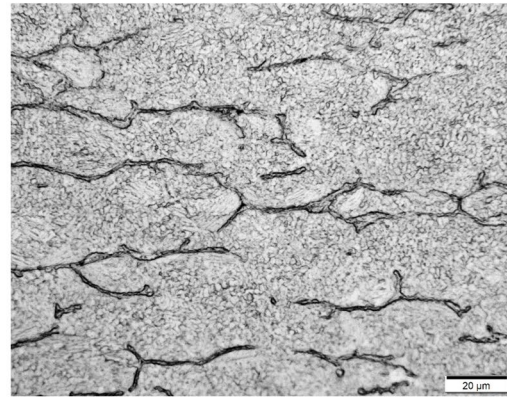
Fig. 6 **a** Optical microscopy image. **b** SEM image of cold sprayed Ti-6Al-4 V structure with the 13% porosity

The microhardness measurements showed an increase in hardness from 298 to 370 HV for CSAM and ISEPT materials, respectively (Fig. 10c). The combined effect of densification and formation of UFG, sourced from dynamic recrystallization, was the reason for an increase in hardness of the ISEPT material. Limited variations in hardness values were observed with an increase in the number of ISEPT passes due to the relatively small grain growth and material reaching to its full density.

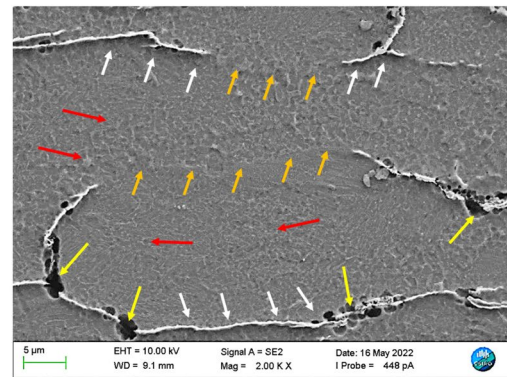
It is worth noting that the ISEPT passes were conducted in air without a protective atmosphere such as inert gas or vacuum. Oxygen substantially affects titanium alloy properties and is mainly used to identify titanium grades [1, 2]. To compare oxygen and nitrogen concentration, LECO analysis was carried out on Ti-6Al-4 V feed stock powder, CSAM material, and the ISEPT sample with six passes. Figure 11 shows that oxygen content of the powder and cold sprayed Ti-6Al-4 V was below 0.2%. An increase in oxygen content from 0.2 to 0.35% was recorded after six ISEPT passes.



(a)



(b)



(c)

Fig. 7 **a** Low magnification optical microscopy, **b** high magnification optical image, and **c** SEM images of CSAM Ti-6Al-4 V after one ISEPT pass at 1.5 kA, 0.7 MPA, and 0.4 mm/s rolling surface speed. The RSB, porosity, and fine grains are shown with white, yellow, and red arrows respectively, and healed splat boundaries are shown with orange arrows

Similarly, CSAM combined with six ISEPT passes increased nitrogen content from 0.01 to 0.11%. These changes in material composition did not increase the material's hardness significantly as presented in Fig. 10c.

EDS analysis after six passes showed uniform distribution of elements (Fig. 12a), without major variations in oxygen concentrations between the splat boundaries and the inner regions of splats (Fig. 12b). The oxygen content was slightly higher than earlier study on CSAM CP-Ti that showed an increase in oxygen content of splat boundaries after 2 ISEPT passes [47]. Nitrogen content however was increased at the splat boundaries compared to inner splat regions, as seen in

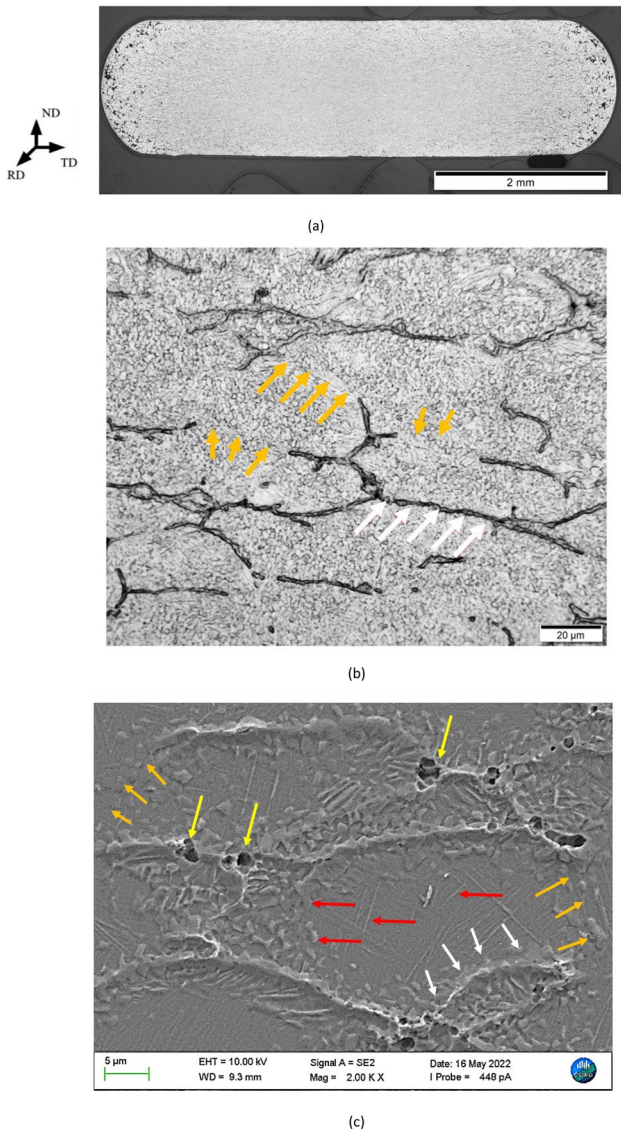


Fig. 8 CSAM Ti-6Al-4 V microstructure after two ISEPT passes. **a** Low magnification optical image, **b** high magnification optical image, and **c** SEM image. Yellow arrows indicate healed splat boundaries and red arrows indicate remnant of splat boundaries. The RSB, porosity, and fine grains are shown with white, yellow, and red arrows respectively, healed splat boundaries are shown with orange arrows

Fig. 12b. The source of nitrogen could be the air trapped in the CSAM porous structure that require further investigation. For example, it would be of interest to establish the relationship between the volume fraction of porosity and its effect on ISEPT Ti-6Al-4 V nitrogen concentration.

3.2 Remnants of splat boundaries (RSB) and microstructure development

The cross-section of ISEPT samples revealed the presence of an elliptical zone in the core of the deformed strip (Fig. 13)

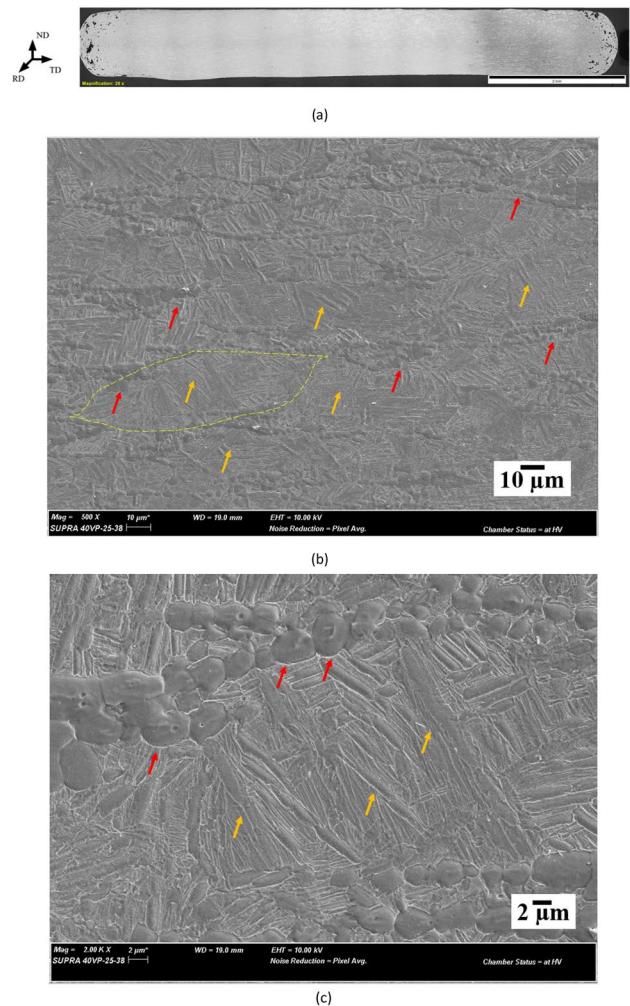


Fig. 9 **a** Low magnification optical microscopy image, **b** SEM image, and **c** high magnification SEM of the equiaxed grain neckling with lamellar interface, for the CSAM Ti-6Al-4 V after six ISEPT passes at 1.5 kA, 0.7 MPa, and 0.4 mm/s rolling surface speed

that was extended with an increase in the number of passes. This area corresponded to a microstructure that was generally RSB-free and without porosity as shown in Fig. 10c. Earlier studies suggested that the formation of this zone is due to uneven strain distribution with higher strain at the centre of material subjected to compression or rolling process [70, 73, 74]. To be able to establish the relationship between the number of passes (i.e. straining) and elimination of RSBs in the microstructure, image analysis was used to measure the area fraction of the dense RSB-free areas in relation to the total area (cross-section) of the ISEPT strip (Fig. 14). It is worth stating that this approach is not precise and was only adopted to obtain an estimate for annihilated cold spray splat boundaries. The RSB content was approximated using image analysis that included additional special etching and polishing procedure explained in “Materials and methods” section of the manuscript.

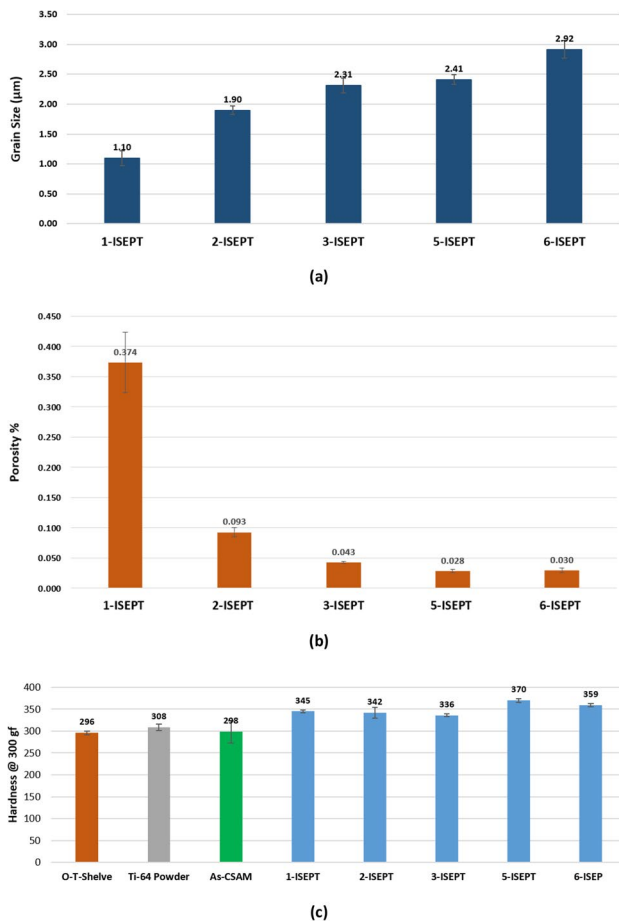
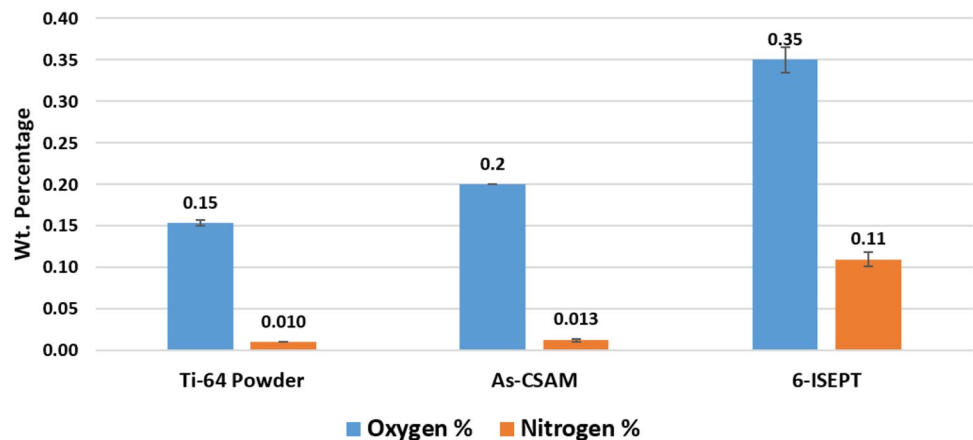


Fig. 10 **a** Measured grain size in relation to number of ISEPT passes, **b** volume fraction of porosity after successive ISEPT passes at the strip core, and **c** the Vickers hardness of the off-the-shelve Ti-6Al-4 V, feed stock powder, as cold sprayed Ti-6Al-4 V, and post ISEPT passes

All optical microscopy images were taken from the strip cross-section perpendicular to the rolling direction. The volume fraction of RSB was significantly reduced from

Fig. 11 Oxygen and nitrogen content of the Ti-6Al-4 V feed stock powder, as-CSAM structure, and after six ISEPT passes



4.9% after the first ISEPT pass to less than 1% in the second pass (Fig. 14). More ISEPT passes reduced the RSB to well below 0.1% confirming almost full transformation of the Ti-6Al-4 V CSAM splat structure to ISEPT induced wrought (recrystallised) structure.

3.3 Tensile properties

Tensile specimens were machined from CSAM and ISEPT strips to assess mechanical properties, as seen in Fig. 15d. Ti-6Al-4 V ISEPT samples after six passes were chosen due to the highest density and volume fraction of recrystallised material. The ISEPT strip presented an average of 1096 MPa ultimate tensile stress (UTS) that was a significant increase from 184 MPa in as-CSAM condition. Two tensile test results are averaged in Fig. 15 a, c. The elongation increased from 1.1% in as-CSAM condition to ~9% after six ISEPT. Grain refinement strengthening is generally observed in UFG structures [37, 72, 75, 76] and explained by the Hall–Petch relationship [37, 72, 75–77]. An earlier study demonstrated that multidirectional forging of Ti-6Al-4 V can produce 1190 MPa and 10.4% ductility from a 0.5 µm UFG material [78]. The ISEPT structure of this study with partially UFG constituents had 1096 MPa UTS that was slightly higher than 989 MPa for OTS Ti-6Al-4 V. Compared to the off-the-shelf (OTS) sample seen in Fig. 15b, the ISEPT-treated sample stress–strain curve seen in Fig. 15a did not have an extended plastic zone that could be due to the combined presence of UFG, lath structure, and higher concentration of the oxygen and nitrogen in the ISEPT material. The achieved UTS was 1069 MPa with 9% elongation that was comparable to previous work on martensitic Ti-6Al-4 V [79]. In that study, 70% warm rolling at 800 °C resulted in 1269 MPa UTS and 13% elongation [79]. Another comparable result was also found on hydrostatic extrusion SPD treatment of Ti-6Al-4 V which resulted in 1180 MPa UTS and 7% elongation [80].

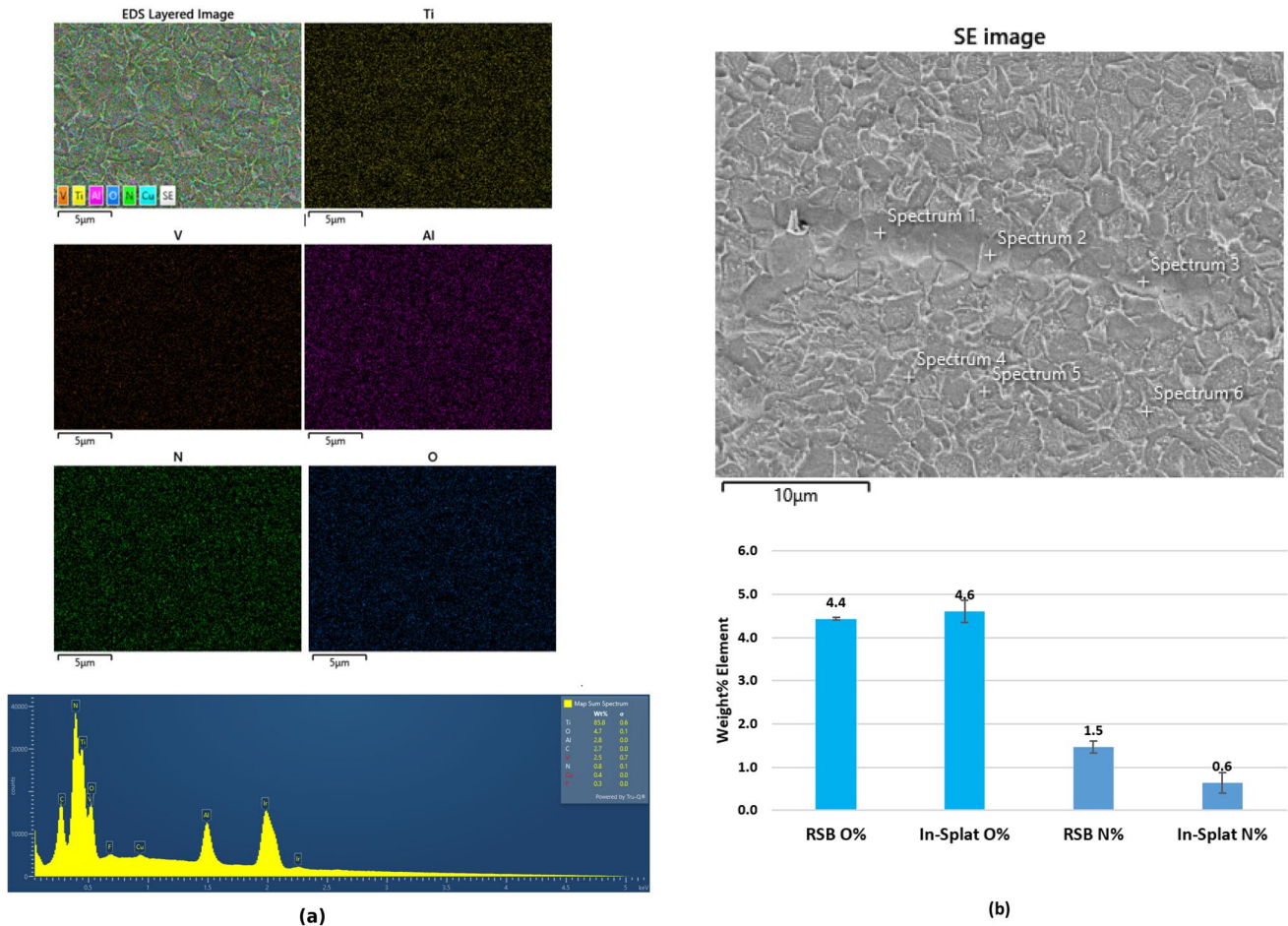


Fig. 12 EDS spectroscopy for six ISEPT pass Ti-6Al-4 V CSAM samples. **a** Element map and **b** oxygen content of selected points (spectrum 1, 2, and 3) on splat boundaries and in-splat regions (spectrum 4, 5, and 6)

The OTS sample presented an ideal ductile fracture surface with cup-cone dimples and macro deformation peaks (yellow arrows) and grain pullouts (red arrows) in Fig. 16a. The CSAM Ti-6Al-4 V fracture surface in Fig. 16b shows a highly porous material with limited bonding between splats. In agreement with CSDT simulations (Fig. 3), this was due to Ti-6Al-4 V particle's insufficient velocity and temperature to achieve the required plastic deformation for densification and bond formation. The ISEPT specimen fracture surface in Fig. 16c reveals the complete elimination of the CSAM splat structure after significant densification from the combined application of current and load. The fracture surface presented fine grains dimple structure with some crystallographic macro-slippage that could contribute to limited ductility of the ISEPT Ti-6Al-4 V, as highlighted with yellow arrows in Fig. 16c. Grain pullouts were similar to OTS material (Fig. 16a) as shown with red arrows in Fig. 16c.

The XRD result (Fig. 17) for the Ti-6Al-4 V feed stock powder confirmed the observations in the SEM image of the powder in Fig. 2b that showed a rapidly cooled material with martensitic/lamellar structure. Two distinct peaks at $2\theta = 39.45$

with 110 plain and $2\theta = 57$ with 200 were chosen to identify the β -phase [81]. The β -phase peaks were not evident in the feedstock due to gas atomised powder rapid cooling. Similarly, after CSAM the original α phase of the powder did not change as expected. In contrast, 110 and 200 peaks were observed in the OTS Stock Ti-6Al-4 V and after six ISEPT passes that confirmed the formation of expected dual $\alpha + \beta$ phase in the Ti-6Al-4 V structure. The XRD quantitative analysis in Fig. 17b reveals a 6.6% β -phase in the OTS Ti-6Al-4 V with slightly lower 5.5 wt% in the ISEPT sample. The CSAM and feed stock samples contained 100 wt% α -phase. The XRD results also revealed the presence of 0.00285 micro-strain in the CSAM material that reduced to 0.00172 after six ISEPT passes.

4 Discussion

Tensile test results in Fig. 15b and porosity measurements in Fig. 10b show significant improvement in cold sprayed Ti-6Al-4 V properties after six ISEPT passes. The ultimate

Fig. 13 Optical image of the ISEPT Ti-6Al-4 V strip cross-section **a** after one pass and **b** after 6 passes, showing estimated high-density RSB-free area in the core

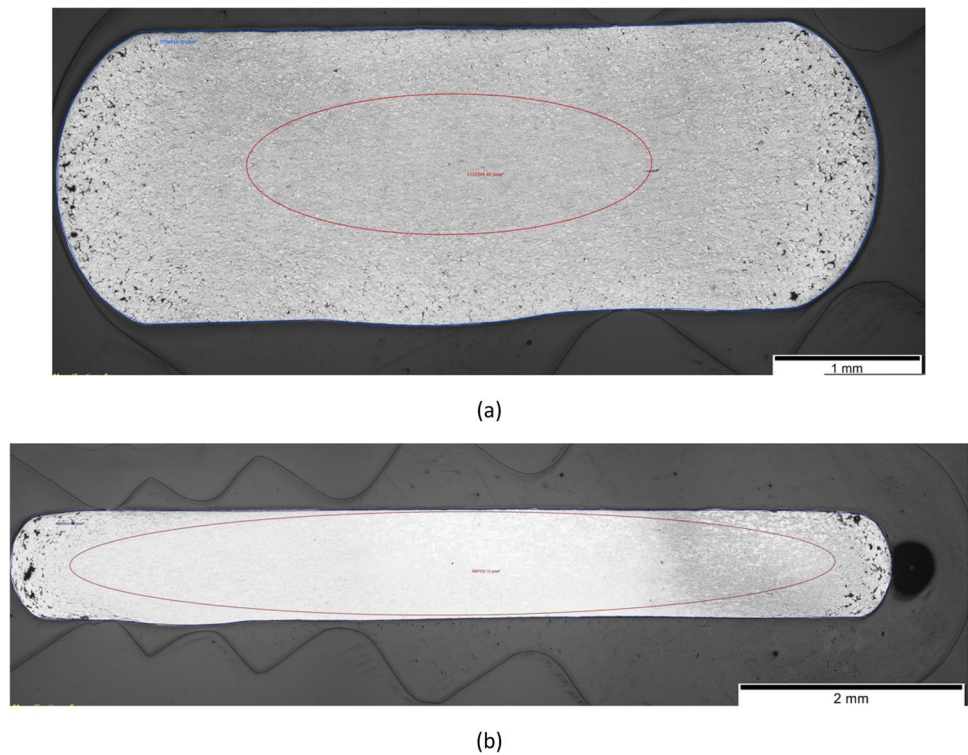
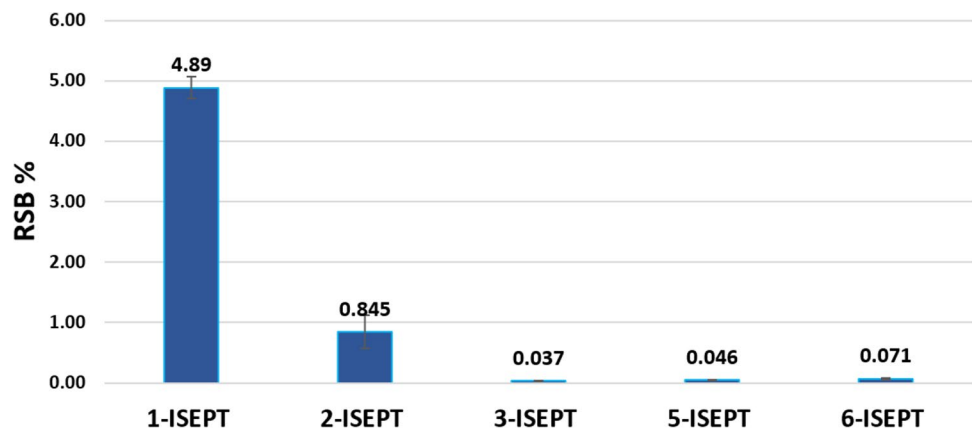


Fig. 14 Estimated volume fraction of RSB as a function of ISEPT passes for CSAM Ti-6Al-4 V of this study

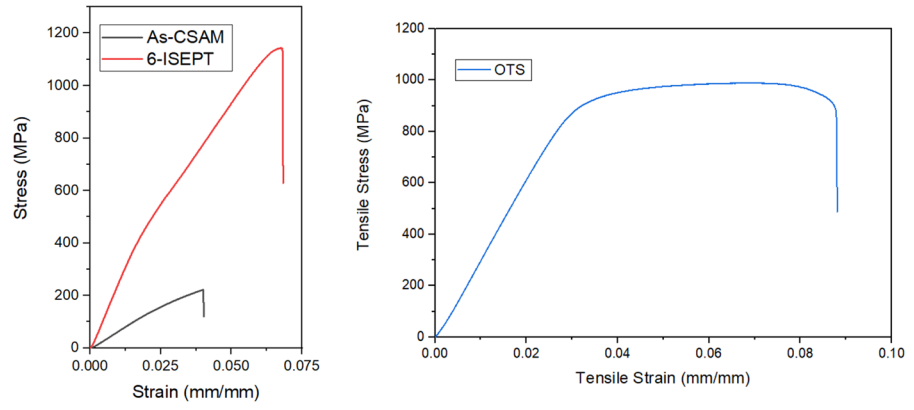


tensile strength of CSAM Ti-6Al-4 V increased from 222 to 1050 MPa after ISEPT. The ductility after ISEPT was increased to 7.3% that was well above the 1.2% for CSAM material. These improvements in mechanical properties were achieved under atmospheric conditions through rapid (i.e. in seconds) transformation of CSAM material under ISEPT simultaneous application of load and current. Dynamic recrystallization in CSAM Ti-6Al-4 V was different from the CSAM CP-Ti in the previous study [47]. For example, the ISEPT processing of the Ti-6Al-4 V produced UFG in the microstructure with more deformation passes required for densification of highly porous cold sprayed strip compared to CP-Ti of previous study [47]. Ti-6Al-4 V resistivity and heat capacity are higher than

CP-Ti [1, 2]. These properties of grade 5 titanium increase Joule heating energy [82], current density, and current application time. The applied electric current and associated electron wind play three important roles which supported rapid recrystallization. First, it provides localised joule heating at crystallographic imperfections including dislocations and grain boundaries. The second effect is the presence of electron wind that assists dislocation motion. Finally, it reduces flow stress by weakening the metallic bond electron cloud [32, 83].

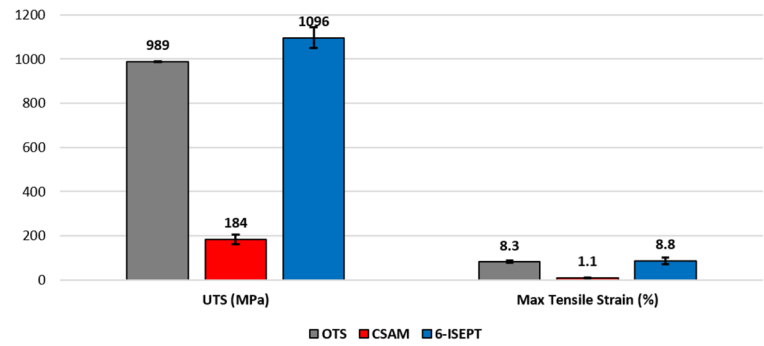
The IR camera temperature measurements during the first two ISEPT passes of CSAM Ti-6Al-4 V were 686 °C and 881 °C consecutively. These temperatures were higher than 428 °C and 440 °C reported in previous work on CSAM

Fig. 15 Comparison of **a** CSAM sample stress–strain curves before and after six ISEPT passes, **b** of the shelf (OTS) wrought Ti-6Al-4 V stress–strain curve, and **c** comparison of the tensile properties for CSAM, ISEPT (6 passes) and OTS Ti-6Al-4 V, **d** photos of the tensile specimens and processing steps of (i–iii) the six-ISEPT CSAM Ti-6Al-4 V, (iv, vi) the as-CSAM Ti-6Al-4 V, (vii, viii) OTS wrought Ti-6Al-4 V, and (ix) comparison of the final equally polished tensile specimens for as-CSAM, OTS, and six-ISEPT materials (top to bottom)

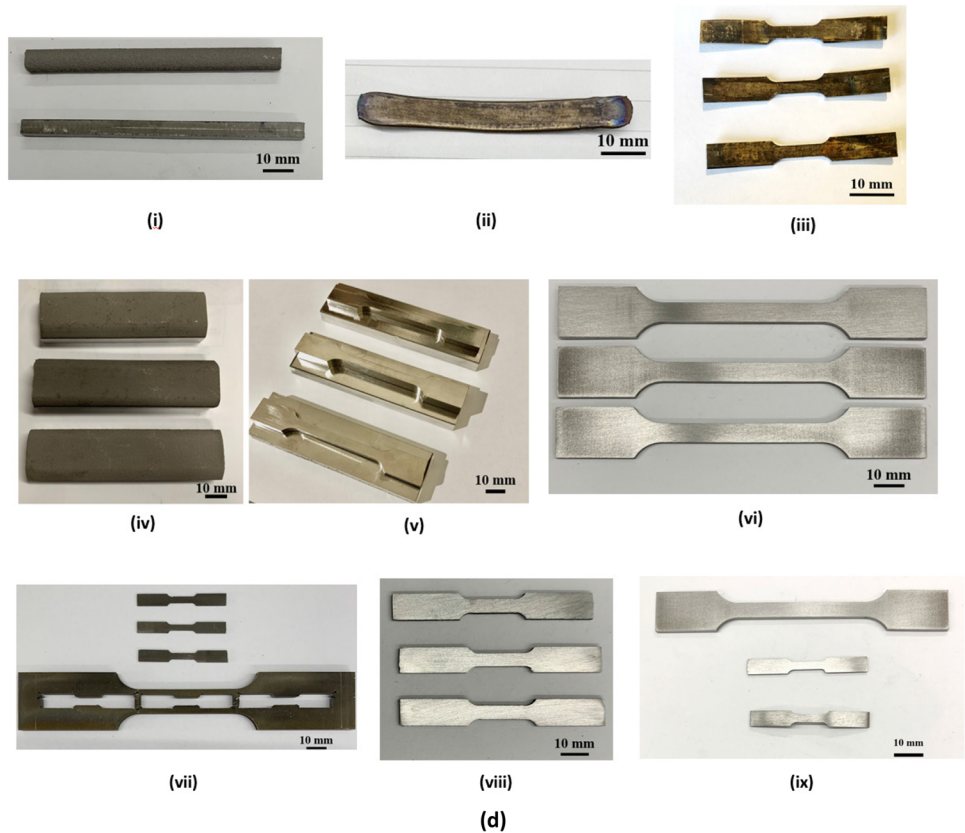


(a)

(b)



(c)

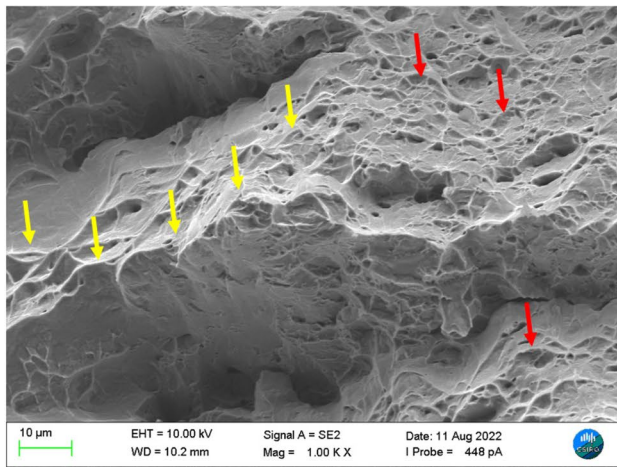


(vii)

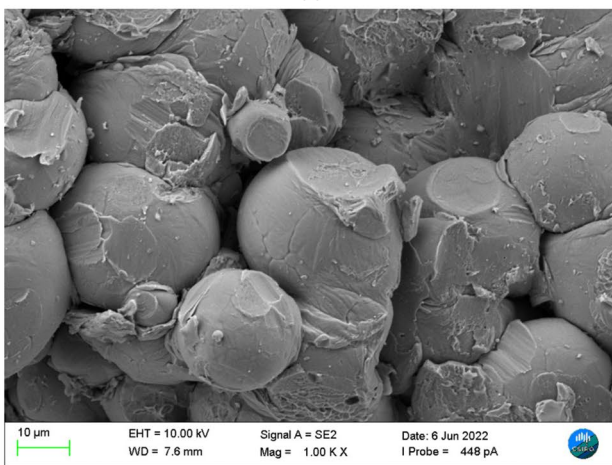
(viii)

(ix)

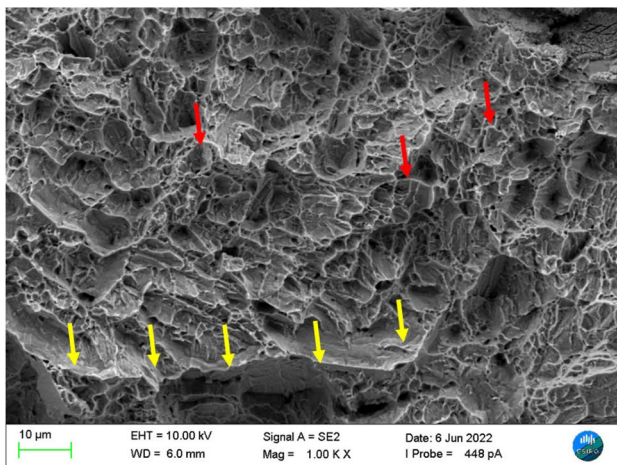
(d)



(a)

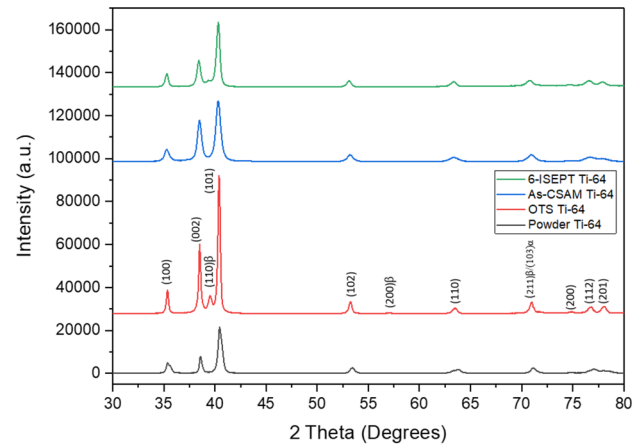


(b)

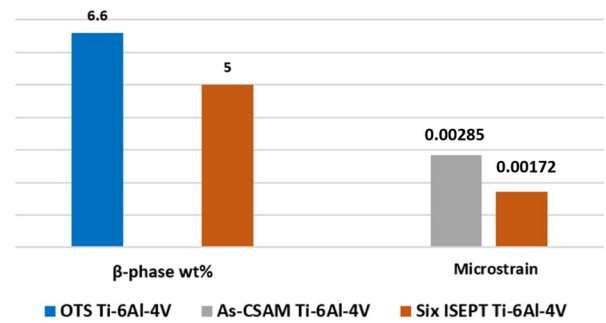


(c)

Fig. 16 SEM images of the tensile specimen fracture surface. **a** Wrought OTS, **b** CSAM, and **c** ISEPT (6 passes) for Ti-6Al-4 V of this study



(a)



(b)

Fig. 17 XRD patterns **a** for Ti-6Al-4 V feed stock powder, OTS, as-CSAM, and ISEPT with 6 passes. **b** Measured fraction of β-phase (wt%) and micro-strain

CP-Ti two ISEPT passes [47]. The increase in temperature with an increase in the number of deformation passes was due to the reduction in sample thickness that led to an increase in current density. Another effect of this was the exposure of the high porosity CSAM Ti-6Al-4 V strip to atmospheric conditions at high deformation temperatures. This led to an increase in oxygen and nitrogen content shown in Fig. 11. This increase in oxygen content however did not result in significant brittleness and formation of alpha-case titanium oxide layer [3, 4], as evident by the tensile properties in Fig. 15. It is highly likely that sufficient reduction of porosity in CSAM deposited material will result in the elimination of oxygen ingress in the ISEPT material that needs further study.

The applied electric current is expected to produce localised heating at macro-crystallographic defect such as splat boundaries, with high dislocation density providing the nucleation site for the growth of the dynamically recrystallised grains [71]. Retarded plastic deformation led to the formation of lamellar structure at the inner regions of splats,

as seen in Fig. 9b. Titanium microstructure generally tends to transform to lamellar morphology when subjected to sufficient thermal energy and time [1].

More ISEPT passes, up to ten, were applied to the strips to investigate the evolution of lamellar microstructure in the absence of sufficient deformation. Figure 18a shows grains at the splat boundaries that resembled necklacing in dynamic recrystallisation (DRX) in materials [68]. In agreement with literature [1], more ISEPT passes led to thicker “basket weave” titanium lamellar laths as shown in Fig. 18b. Similarly, the size of these colonies was increased (highlighted with yellow dashed lines) due to Joule thermal heating in the absence of deformation (Fig. 18b). The application of more passes led to the expansion of lamellar titanium at the expense of DRX grains as presented in Fig. 18c. This suggests that limited deformation of the strip after 10 passes allows for domination of heating and rapid cooling for microstructure evolution preventing the progress of dynamic recrystallisation.

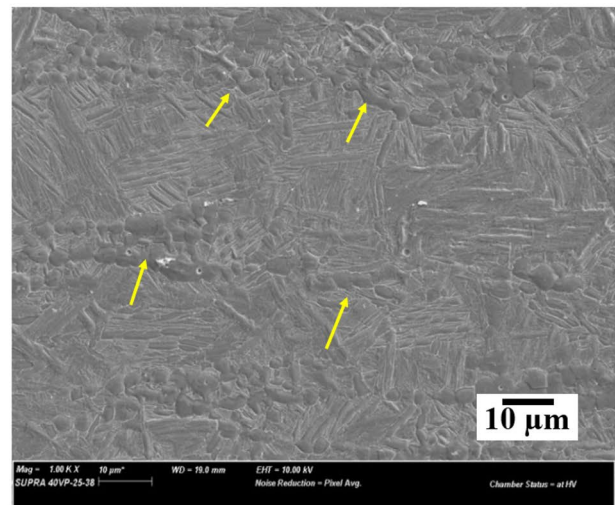
The absence of 110 and 200 peaks confirmed that the β phase was consumed by the α phase with an increase in the number of passes from 6 to 10 when deformation and driving force for dynamic recrystallisation was limited due to the reduction in strip's thickness under constant applied load of this study, as seen in Fig. 19.

The oxygen and nitrogen content after ten ISEPT passes were measured as 0.57% and 0.32%, respectively. This significant rise could be due to a reduction in strip thickness contributing to overheating that facilitates oxygen and nitrogen absorption from surrounding air. A systematic study is required to confirm this. Results suggest that optimising the ISEPT treatment by reducing the porosity in CSAM structure may result in fewer ISEPT passes for densification with the advantage to reduce oxygen absorption.

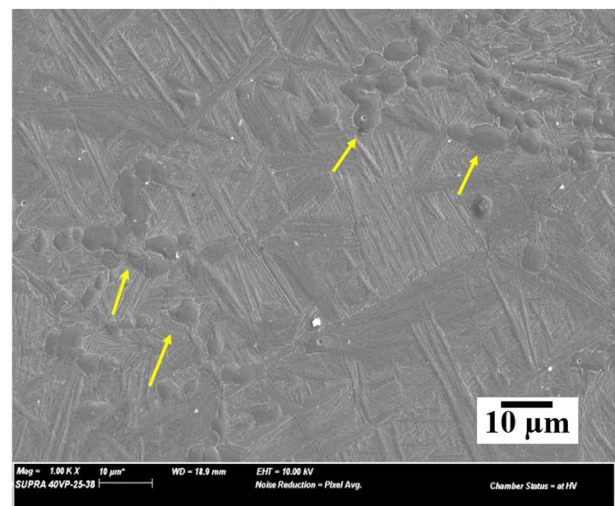
5 Conclusions

The rapid and energy-efficient ISEPT thermomechanical treatment in processing cold spray AM structures is a critical part of this manufacturing process. This article presented the application of this novel electroplastic treatment process as the potential method to broaden the use of titanium structures in large-scale industrial applications. The key results and observations from this work are presented in the following points:

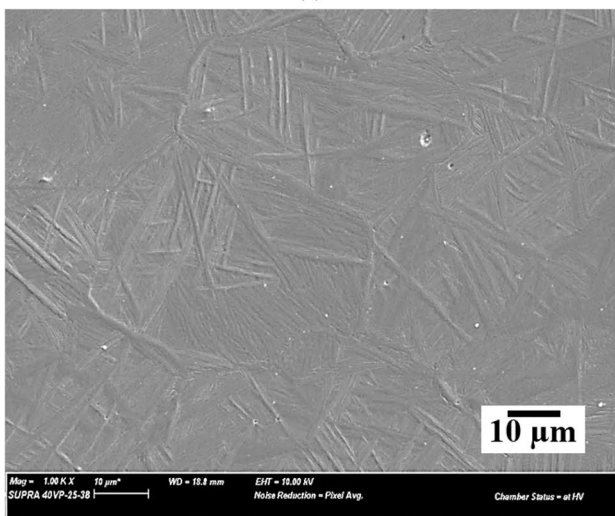
- Results showed that ISEPT simultaneously densifies and improves mechanical properties of the CSAM Ti-6Al-4V.



(a)



(b)



(c)

Fig. 18 Microstructure evolution of Ti-6Al-4 V after **a** six, **b** eight, and **d** ten ISEPT passes

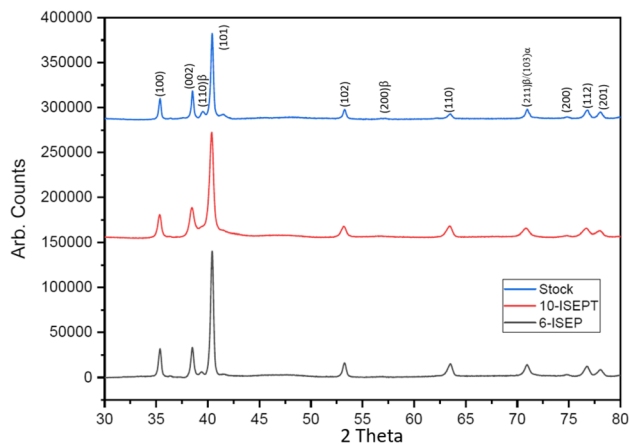


Fig. 19 Comparison of the XRD patterns for Ti-6Al-4 V CSAM after six and ten ISEPT passes in relation to OTS Ti-6Al-4 V

- For conditions of this study, Ti-6Al-4V feed stock powder had approximately three times the strength and hardness compared to commercially pure titanium powder which led to double the porosity for initial as-CSAM structure, with more ISEPT passes for densification.
- The Cold Spray Digital Twin simulation results revealed the critical particle velocities were high enough to produce good CSAM deposition efficiency but not sufficient enough to produce sufficient particle deformation and interlocking to achieve high-density CSAM Ti-6Al-4V.
- Compared to CP-Ti, the higher strength of Ti-6Al-4V powder led to an increase in CSAM porosity and a higher number of ISEPT passes required for the densification and elimination of the RSB.
- Six ISEPT passes with an initial current density of 27 Amp/mm², 0.7 MPa load, and 0.02 s⁻¹ stain rate produced a total accumulative reduction of 68% that nearly eliminated 13% porosity of the CSAM Ti-6Al-4V to 0.03%.
- The ductility of as-CSAM was considerably improved from 1.1 to 8.8% after six ISEPT passes that created ~3 μm UFG structure and resulted in improvement in ultimate tensile strength (1096 MPa) for Ti-6Al-4V similar to OTS (~990 MPa) material.
- Analysis of splat boundaries healing during the successive ISEPT passes showed incremental elimination of RSB with the growth of RSB-free area at the centre of sample cross-section.
- The synergy of concurrent application of electric current (electron wind) and deformational load led to localised transformation and rapid nucleation and growth of dynamically recrystallised grains that was more pronounced at splat boundaries.
- Future research directions include further optimization of ISEPT treatments via increasing the applied load to

reduce the number of passes and exposure to air during deformation. This requires careful study on the impact of changing sample's resistance value with applied current. Long-term research directions include ISEPT treatment of other low-formability cold spray deposits such as stainless steel, Inconel, and magnesium.

Acknowledgements The authors would like to thank and acknowledge the technical and scientific assistance of Emma Regos, Roshan Dodanwala, Malisja de Vries, Mark Greaves, and Aaron Seeber from CSIRO, Clayton, Victoria; and Rizwan Abdul Rahman Rashid, Novana Hutasoit, Girish Thipperudrappa, and Aidan O'Keeffe from Swinburne University of Technology, Hawthorn, Victoria.

Author contribution Mohammed Abdul Khalik (MAK): contributed towards carrying out the research work and writing the manuscript. Saden H. Zahiri: concept development and initial experimental work co-supervision and contribution towards the manuscript. Syed H. Masood: primary supervisor of this project working with MAK and contribution towards manuscript. Suresh Palanisamy: co-supervisor of MAK, contribution towards materials characterisation, and writing of the manuscript. Stefan Gulizia: concept development and co-supervision. M. Faizan-Ur-Rab: contributed towards carrying out CFD simulations in relation to Cold Spray Digital Twin.

Funding Open Access funding enabled and organized by CAUL and its Member Institutions This project is funded by the Commonwealth Scientific and Industrial Research Organisation (CSIRO), Victoria, Australia, and the Swinburne University of Technology, Victoria, Australia.

Data availability The raw/processed data and materials required to reproduce these findings cannot be shared at this time as the data also forms part of an ongoing study.

Declarations

Ethical approval There are no requirements for ethical approval for this project.

Consent to participate All the authors consent to participate towards this work.

Consent for publication All authors contributed towards this work and publication in this journal.

Conflict of interest The authors declare no competing interests.

Open Access This article is licensed under a Creative Commons Attribution 4.0 International License, which permits use, sharing, adaptation, distribution and reproduction in any medium or format, as long as you give appropriate credit to the original author(s) and the source, provide a link to the Creative Commons licence, and indicate if changes were made. The images or other third party material in this article are included in the article's Creative Commons licence, unless indicated otherwise in a credit line to the material. If material is not included in the article's Creative Commons licence and your intended use is not permitted by statutory regulation or exceeds the permitted use, you will need to obtain permission directly from the copyright holder. To view a copy of this licence, visit <http://creativecommons.org/licenses/by/4.0/>.

References

- Lütjering G, Williams JC (2007) Titanium. Springer-Verlag, Berlin Heidelberg. <https://doi.org/10.1007/978-3-540-73036-1>
- Leyens C, Peters M (2003) Titanium and titanium alloys: fundamentals and applications. WILEY-VCH Verlag GmbH & Co KGaA, Weinheim. <https://doi.org/10.1002/3527602119>
- Sefer B (2014) Oxidation and alpha-case phenomena in titanium alloys used in aerospace industry: Ti–6Al–2Sn–4Zr–2Mo and Ti–6Al–4V. (Doctoral dissertation) Luleå University of Technology, Sweden
- Sung S-Y, Han B-S, Kim Y-J (2012) Formation of alpha case mechanism on titanium investment cast parts. In: Nurul Amin (eds) Titanium Alloys, pp 29–42. <https://doi.org/10.5772/35496>
- Zahiri SH, Gulizia S, Prentice L (2020) An overview of cold spray additive technology in Australia for melt-less manufacture of titanium. In: MATEC Web of Conferences, vol 321. EDP Sciences, p 03011. <https://doi.org/10.1051/mateconf/202032103011>
- Li W, Cao C, Wang G, Wang F, Xu Y, Yang X (2019) ‘Cold spray+’ as a new hybrid additive manufacturing technology: a literature review. *Sci Technol Weld Joining* 24(5):420–445
- Li W, Cao C, Yin S (2020) Solidstate cold spraying of Ti and its alloys: a literature review. *Prog Mater Sci* 110:100633. <https://doi.org/10.1016/j.pmatsci.2019.100633>
- Yin S, Cavaliere P, Aldwell B, Jenkins R, Liao H, Li W, Lupoi R (2018) Cold spray additive manufacturing and repair: fundamentals and applications. *Addit Manuf* 21:628–650
- Assadi H, Kreye H, Gärtner F, Klassen T (2016) Cold spraying—a materials perspective. *Acta Mater* 116:382–407
- Assadi H, Schmidt T, Richter H, Kliemann JO, Binder K, Gärtner F, Klassen T, Kreye H (2011) On parameter selection in cold spraying. *J Therm Spray Technol* 20(6):1161–1176
- Schmidt T, Assadi H, Gärtner F, Richter H, Stoltenhoff T, Kreye H, Klassen T (2009) From particle acceleration to impact and bonding in cold spraying. *J Therm Spray Technol* 18(5):794–808
- Schmidt T, Gärtner F, Assadi H, Kreye H (2006) Development of a generalized parameter window for cold spray deposition. *Acta Mater* 54(3):729–742
- Assadi H, Gärtner F, Stoltenhoff T, Kreye H (2003) Bonding mechanism in cold gas spraying. *Acta Mater* 51(15):4379–4394
- Zahiri SH, Gulizia S (2021) Process for forming wrought structures using cold spray. In: World international property organization, U.S. Patent Application No. 16/624,741
- Zahiri SH, Phan TD, Masood SH, Jahedi M (2014) Development of holistic three-dimensional models for cold spray supersonic jet. *J Therm Spray Technol* 23(6):919–933
- Zahiri SH, Fraser D, Jahedi M (2009) Recrystallization of cold spray-fabricated CP titanium structures. *J Therm Spray Technol* 18(1):16–22
- Zahiri SH, Fraser D, Gulizia S, Jahedi M (2006) Effect of processing conditions on porosity formation in cold gas dynamic spraying of copper. *J Therm Spray Technol* 15(3):422–430
- Wong W, Rezaeian A, Irissou E, Legoux JG, Yue S (2010) Cold spray characteristics of commercially pure Ti and Ti–6Al–4V. In: Advanced materials research, vol 89. Trans Tech Publications Ltd., pp. 639–644. <https://doi.org/10.4028/www.scientific.net/AMR.89-91.639>
- Zahiri SH, Antonio CI, Jahedi M (2009) Elimination of porosity in directly fabricated titanium via cold gas dynamic spraying. *J Mater Process Technol* 209(2):922–929
- Vo P, Irissou E, Legoux JG, Yue S (2013) Mechanical and microstructural characterization of cold-sprayed Ti–6Al–4V after heat treatment. *J Therm Spray Technol* 22(6):954–964
- Vo P, Goldbaum D, Wong W, Irissou E, Legoux J-G, Chromik RR, Yue S (2015) Cold-spray processing of titanium and titanium alloys. *Titanium Powder Metallurgy*. Elsevier, pp 405–423
- Khun NW, Tan AWY, Sun W, Liu E (2017) Effect of heat treatment temperature on microstructure and mechanical and tribological properties of cold sprayed Ti–6Al–4V coatings. *Tribol Trans* 60(6):1033–1042
- MacDonald D, Fernández R, Delloro F, Jodoin B (2017) Cold spraying of armstrong process titanium powder for additive manufacturing. *J Therm Spray Technol* 26(4):598–609
- Li Z, Yang X, Zhang J, Shan A (2016) Interfacial mechanical behavior and electrochemical corrosion characteristics of cold-sprayed and hot-rolled titanium/stainless-steel couples. *Adv Eng Mater* 18(7):1240–1249
- Zhao Z, Tang J, Jia C, Qiu X, Ren Y, Liu H, Shen Y, Du H, Cui X, Wang J (2020) Microstructural evolutions and mechanical characteristics of Ti/steel clad plates fabricated through cold spray additive manufacturing followed by hot-rolling and annealing. *Mater Des* 185:108249
- Petrovskiy P, Sova A, Doubenskaia M, Smurov I (2019) Influence of hot isostatic pressing on structure and properties of titanium cold-spray deposits. *Int J Adv Manuf Technol* 102(1–4):819–827
- Bocanegra-Bernal MH (2004) Hot isostatic pressing (HIP) technology and its applications to metals and ceramics. *J Mater Sci* 39(21):6399–6420
- Ivasishin OM, Lütjering G (1993) Structure and mechanical properties of high-temperature titanium alloys after rapid heat treatment. *Mater Sci Eng, A* 168(1):23–28
- Yanagimoto J, Izumi R (2009) Continuous electric resistance heating—hot forming system for high-alloy metals with poor workability. *J Mater Process Technol* 209(6):3060–3068
- Saifullin RN, Natalenko VS (2011) A method of production of sintered strips by electric resistance rolling. *Weld Int* 25(03):205–208
- Chen Z, Ding H, Chen R, Guo J, Fu H (2019) An innovation for microstructural modification and mechanical improvement of TiAl alloy via electric current application. *Sci Rep* 9(1):1–10
- Salandro WA, Jones JJ, Bunget C, Mears L, Roth JT (2014) Electrically assisted forming. In: Modeling and control. Springer, Switzerland, p 355
- Kinsey B, Cullen G, Jordan A, Mates S (2013) Investigation of electroplastic effect at high deformation rates for 304SS and Ti–6Al–4V. *CIRP Ann* 62(1):279–282
- Ivasishin OM, Teliovich RV (1999) Potential of rapid heat treatment of titanium alloys and steels. *Mater Sci Eng, A* 263(2):142–154
- Ivasishin OM, Markovsky PE (1996) Enhancing the mechanical properties of titanium alloys with rapid heat treatment. *Jom* 48(7):48–52
- Ivasishin OM, Semiatin SL, Markovsky PE, Shevchenko SV, Ulshin SV (2002) Grain growth and texture evolution in Ti–6Al–4V during beta annealing under continuous heating conditions. *Mater Sci Eng, A* 337(1–2):88–96
- Ivasishin OM (2001) High strength microstructural forms developed in titanium alloys by rapid heat treatment. *Le Journal de Physique IV*, 11(PR4), Pr4-233. <https://doi.org/10.1051/jp4:2001429>
- Bhosle SM, Friedrich CR (2017) Rapid heat treatment for anatase conversion of titania nanotube orthopedic surfaces. *Nanotechnology* 28(40):405603
- Ozturk F, Ece RE, Polat N, Koksak A (2011) Assessment of electrical resistance heating for hot formability of Ti–6Al–4V alloy sheet. *Key Eng Mater* 473:130–136
- Chong Y, Bhattacharjee T, Yi J, Shibata A, Tsuji N (2017) Mechanical properties of fully martensite microstructure in Ti–6Al–4V alloy transformed from refined beta grains obtained by rapid heat treatment (RHT). *Scripta Mater* 138:66–70

41. Delville R, Malard B, Pilch J, Sittner P, Schryvers D (2010) Microstructure changes during non-conventional heat treatment of thin Ni–Ti wires by pulsed electric current studied by transmission electron microscopy. *Acta Mater* 58(13):4503–4515
42. Miura F, Mogi M, Ohura Y (1988) Japanese NiTi alloy wire: use of the direct electric resistance heat treatment method. *Eur J Orthod* 10(1):187–191
43. Salandro WA, Jones JJ, Bunget C, Mears L, Roth JT (2015) Macroscale modeling of the electroplastic effect. electrically assisted forming. Springer, pp 55–82
44. Lee M, Yu J, Bae MH, Won JW, Lee T (2021) Accelerated recrystallization behavior of commercially pure titanium subjected to an alternating-current electropulse. *J Market Res* 15:5706–5711
45. Lee CH, Choi S-W, Narayana PL, Nguyet Nguyen TA, Hong S-T, Kim JH, Kang N, Hong J-K (2021) Effect of electric current heat treatment on commercially pure titanium sheets. *Metals* 11(5):783
46. Khalik MA, Zahiri SH, Masood SH, Palanisamy S, Gulizia S (2021) In situ electro-plastic treatment for thermomechanical processing of CP titanium. *The Int J Adv Manuf Technol* 115(7–8):2639–2657. <https://doi.org/10.1007/s00170-021-07342-6>
47. Khalik MA, Zahiri SH, Palanisamy S, Masood SH, Gulizia S, Faizan-Ur-Rab M (2022) Rapid elimination of porosity and brittleness in cold spray additive manufactured grade 2 titanium via in situ electro-plastic treatment. *Int J Adv Manuf Technol* 119:1–16. <https://doi.org/10.1007/s00170-021-08309-3>
48. Grimm TJ, Mears LM (2022) Skin effects in electrically assisted manufacturing. *Manuf Lett* 34:67–70
49. Xu Z, Jiang T, Huang J, Peng L, Lai X, Fu MW (2022) Electroplasticity in electrically-assisted forming: process phenomena, performances and modelling. *Int J Mach Tools Manuf* 175:103871
50. Yin F, Ma S, Hu S, Liu Y, Hua L, Cheng GJ (2023) Understanding the microstructure evolution and mechanical behavior of titanium alloy during electrically assisted plastic deformation process. *Mater Sci Eng A* 869:144815. <https://doi.org/10.1016/j.msea.2023.144815>
51. Dong H-R, Li X-Q, Li Y, Wang Y-H, Wang H-B, Peng X-Y, Li D-S (2022) A review of electrically assisted heat treatment and forming of aluminum alloy sheet. *Int J Adv Manuf Technol* 120(11–12):7079–7099
52. Guo A, Kong D, Zhou X, Kong H, Qu P, Wang S, Wang H, Hu Y (2022) Method for preparing damage-resistant 3D-printed ceramics via interior-to-exterior strengthening and toughening. *Addit Manuf* 60:103272
53. Guo S, Wang M, Sui S, Li J, Chen H, Hao X, Zhao X, Lin X (2022) Research on optimizing strength and ductility of HfNbTaZr dual-phase high-entropy alloy by tuning chemical short-range order. *Int J Refract Metal Hard Mater* 108:105942
54. Faizan-Ur-Rab M, Zahiri SH, Masood SH, Jahedi M, Nagarajah R (2017) PIV validation of 3D multicomponent model for cold spray within nitrogen and helium supersonic flow field. *J Therm Spray Technol* 26(5):941–957
55. Faizan-Ur-Rab M, Zahiri SH, King PC, Busch C, Masood SH, Jahedi M, Nagarajah R, Gulizia S (2017) Utilization of titanium particle impact location to validate a 3D multicomponent model for cold spray additive manufacturing. *J Therm Spray Technol* 26(8):1874–1887
56. Faizan-Ur-Rab M, Zahiri SH, Masood SH, Jahedi M, Nagarajah R (2016) 3D CFD multicomponent model for cold spray additive manufacturing of titanium particles. *CFD Modeling and Simulation in Materials Processing* 2016. Springer, pp 213–220
57. Faizan-Ur-Rab M, Zahiri SH, Masood SH, Phan TD, Jahedi M, Nagarajah R (2016) Application of a holistic 3D model to estimate state of cold spray titanium particles. *Mater Des* 89:1227–1241
58. Rab MFU, Zahiri S, Masood SH, Jahedi M, Nagarajah R (2015) Development of 3D multicomponent model for cold spray process using nitrogen and air. *Coatings* 5(4):688–708
59. Grotjans H, Menter F (1998) Wall Functions for General Application CFD Codes. In: *Proceedings of the 4th European Computational Fluid Dynamics Conference*. John Wiley & Sons, Chichester, pp 1112–1117
60. Wilcox DC (1998) *Turbulence modeling for CFD*, vol 2. DCW industries, La Canada, CA, pp 103–217
61. Karimi M, Fartaj A, Rankin G, Vanderzwet D, Birtch W, Villafuerte J (2006) Numerical simulation of the cold gas dynamic spray process. *J Therm Spray Technol* 15(4):518–523
62. Meyer M, Lupoi R (2015) An analysis of the particulate flow in cold spray nozzles. *Mech Sci* 6(2):127–136
63. Samareh B, Dolatabadi A (2007) A three-dimensional analysis of the cold spray process: the effects of substrate location and shape. *J Therm Spray Technol* 16(5–6):634–642
64. Bai S, Perevoshchikova N, Sha Y, Wu X (2019) The effects of selective laser melting process parameters on relative density of the AlSi10Mg parts and suitable procedures of the archimedes method. *Appl Sci* 9(3):583
65. Kumar K, Pooleery A, Madhusoodanan K, Singh RN, Chakravarty JK, Dutta BK, Sinha RK (2014) Use of miniature tensile specimen for measurement of mechanical properties. *Procedia Eng* 86:899–909
66. Kraemer DM, Polvorosa R, De Lacalle LNL, Alonso-Pinillos U, Abate G, Riu F (2016) Alternatives for specimen manufacturing in tensile testing of steel plates. *Exp Tech* 40(6):1555–1565
67. Silva CA, Rosa PAR, Martins PAF (2016) Innovative testing machines and methodologies for the mechanical characterization of materials. *Exp Tech* 40(2):569–581
68. Lütjering G, Williams JC, James C (2007) *Alpha + Beta Alloys*. In: *Titanium. Engineering Materials, Processes*. Springer, Berlin, Heidelberg
69. Zhang ZX, Qu SJ, Feng AH, Shen J, Chen DL (2017) Hot deformation behavior of Ti-6Al-4V alloy: Effect of initial microstructure. *J Alloy Compd* 718:170–181
70. Souza PM, Beladi H, Singh RP, Hodgson PD, Rolfe B (2018) An analysis on the constitutive models for forging of Ti6Al4V alloy considering the softening behavior. *J Mater Eng Perform* 27(7):3545–3558
71. Humphreys, F.J. and M. Hatherly, *Recrystallization and related annealing phenomena*. 2012: Elsevier. <https://doi.org/10.1016/B978-0-08-044164-1.X5000-2>
72. Chao Q, Hodgson P, Beladi H (2014) Microstructure evolution of martensitic Ti-6Al-4V alloy during warm deformation. In: *Materials Science Forum*. vol 783. Trans Tech Publications Ltd., pp 679–684. <https://doi.org/10.4028/www.scientific.net/MSF.783-786.679>
73. Pope J, Jackson M (2019) FAST-forge of diffusion bonded dissimilar titanium alloys: a novel hybrid processing approach for next generation near-net shape components. *Metals* 9(6):654
74. Zhuchkova T, Shkatov V, Mazur I, Aksenov S (2018) Comparison of results of dynamic recrystallization research of HC420LA steel by two types of tests on Gleeble 3800. *J Chem Technol Metall* 53:354–359
75. Wu H, Jiang J, Liu H, Sun J, Gu Y, Tang R, Zhao X, Ma A (2017) Fabrication of an ultra-fine grained pure titanium with high strength and good ductility via ECAP plus cold rolling. *Metals* 7(12):563
76. Zhao Y, Guo H, Fu MW, Ning Y, Yao Z (2013) Fabrication of bulk ultrafine grained titanium alloy via equal channel angular pressing based thermomechanical treatment. *Mater Des* 46:889–894
77. Hansen N (2004) Hall-Petch relation and boundary strengthening. *Scripta Mater* 51(8):801–806
78. Zhang ZX, Qu SJ, Feng AH, Shen J (2017) Achieving grain refinement and enhanced mechanical properties in Ti-6Al-4V alloy produced by multidirectional isothermal forging. *Mater Sci Eng, A* 692:127–138

79. Chao Q, Cizek P, Wang J, Hodgson PD, Beladi H (2016) Enhanced mechanical response of an ultrafine grained Ti–6Al–4V alloy produced through warm symmetric and asymmetric rolling. *Mater Sci Eng, A* 650:404–413
80. Zhrebtsov S, Mazur A, Salishchev G, Lojkowski W (2008) Effect of hydrostatic extrusion at 600–700° C on the structure and properties of Ti–6Al–4V alloy. *Mater Sci Eng, A* 485(1–2):39–45
81. Da Silva SLR, Kerber LO, Amaral L, Dos Santos CA (1999) X-ray diffraction measurements of plasma-nitrided Ti–6Al–4V. *Surf Coat Technol* 116:342–346
82. Li W, Wu D, Hu K, Xu Y, Yang X, Zhang Y (2021) A comparative study on the employment of heat treatment, electric pulse processing and friction stir processing to enhance mechanical properties of cold-spray-additive-manufactured copper. *Surf Coat Technol* 409:126887
83. Maccari F, Karpenkov DY, Semenova E, Karpenkov AY, Radulov IA, Skokov KP, Gutfleisch O (2020) Accelerated crystallization and phase formation in Fe40Ni40B20 by electric current assisted annealing technique. *J Alloys Compd* 836:155338. <https://doi.org/10.1016/j.jallcom.2020.155338>

Publisher's note Springer Nature remains neutral with regard to jurisdictional claims in published maps and institutional affiliations.